



Electrical promotion of spatially photoinduced charge separation via interfacial-built-in quasi-alloying effect in hierarchical $Zn_2In_2S_5/Ti_3C_2(O, OH)_x$ hybrids toward efficient photocatalytic hydrogen evolution and environmental remediation

Hou Wang^a, Yuanmiao Sun^b, Yan Wu^a, Wenguang Tu^a, Shuyang Wu^a, Xingzhong Yuan^c, Guangming Zeng^c, Zhichuan J. Xu^b, Shuzhou Li^b, Jia Wei Chew^{a,d,*}

^a School of Chemical and Biomedical Engineering, Nanyang Technological University, 637459, Singapore

^b School of Materials Science and Engineering, Nanyang Technological University, 639798 Singapore

^c College of Environmental Science and Engineering, Hunan University, Changsha 410082, PR China

^d Singapore Membrane Technology Center, Nanyang Environment and Water Research Institute, Nanyang Technological University, 639798, Singapore



ARTICLE INFO

Keywords:

Solar conversion

$Zn_2In_2S_5$

$Ti_3C_2(O$

$OH)_x$

Interface

Built-in quasi-alloying effect

ABSTRACT

Exploring new hybridized catalysts for synergistically promoting the photocatalytic efficiency hold great challenges in solar-to-chemical energy conversion and environmental remediation. Hierarchical $Zn_2In_2S_5/Ti_3C_2(O, OH)_x$ hybrids have been rationally constructed using $Ti_3C_2(O, OH)_x$ as a two-dimensional platform for *in situ* growth of flower-like $Zn_2In_2S_5$ microsphere under anaerobically hydrothermal conditions. Upon exposure to visible light, the $Zn_2In_2S_5/Ti_3C_2(O, OH)_x$ hybrids with the $Ti_3C_2(O, OH)_x$ content of 1.5% (by mass) had hydrogen generation yields of $12,983.8 \mu\text{mol g}^{-1}$, which was significantly better than that of pure $Zn_2In_2S_5$. The apparent quantum efficiency reached 8.96% at 420 nm. Furthermore, the photocatalytic tetracycline removal rate was 1.25 times higher than that of pure $Zn_2In_2S_5$, and can be further improved with the increase of temperature in the range of 35–55 °C. Excellent photocatalytic activity originated from the synergistic effects between visible-light-active $Zn_2In_2S_5$ and conductive $Ti_3C_2(O, OH)_x$ for spatial electrical promotion. The photogenerated-electrons transfer efficiency from $Zn_2In_2S_5$ to $Ti_3C_2(O, OH)_x$ was 33.0%. In accordance with spectroscopic, electrochemical, and density functional theory studies, we proposed that the interfacial-built-in quasi-alloying effect between ZIS and $Ti_3C_2(O, OH)_x$ culminated in notable charge redistribution, which thereby facilitated the spatial separation and transfer of photogenerated electron-hole pairs. This work revealed the underlying photo-excited charge transfer between metallic compound and semiconductor.

1. Introduction

Solar conversion is a promising and sustainable source of energy for environmental remediation [1,2]. Since the photoelectrochemical solar energy conversion of titanium dioxide (TiO_2) reported by Fujishima and Honda [3], numerous new photocatalysts have sprung up with potential impact for practical applications, including metal sulfide, two dimensional (2D) polymeric carbon nitride, metal-organic frameworks, covalent organic framework and perovskite [4–10]. A perfect photocatalyst should have a narrow band-gap with excellent solar absorption, highly-efficient charge spatial separation, and favorable band level for allowing for enough photoinduced electrons and holes with suitable potential to participate in redox reaction [11]. Recently, the ternary

chalcogenides like $Zn_{m}In_2S_{3+m}$ ($m = 1–5$) aroused much interest in the field of photocatalysis due to beneficial electronic characteristics, band-gaps and band-edges, tunable optical properties and defective structure [12].

Different ternary $Zn_{m}In_2S_{3+m}$ phases with polytypic modifications consist of m layers of S-Zn-S and a repeating structural unit (S-In(o)-S-In(t)S(◊)S). In slightly distorted layer structure with close packing, the indium atom layers are octahedral (o) and tetrahedral (t) sites with the vacant (◊) cationic sites between S atom layers [13]. The highest occupied molecular orbital (HOMO) levels of $ZnIn_2S_4$ are dependent on the hybridized orbitals of the S3p and Zn3d, while the hybridized In5s5p and S3p orbitals mainly determine the lowest unoccupied molecular orbital (LUMO) levels [14,15]. Therefore, electronic

* Corresponding author at: School of Chemical and Biomedical Engineering, Nanyang Technological University, 637459, Singapore.

E-mail address: JChew@ntu.edu.sg (J.W. Chew).

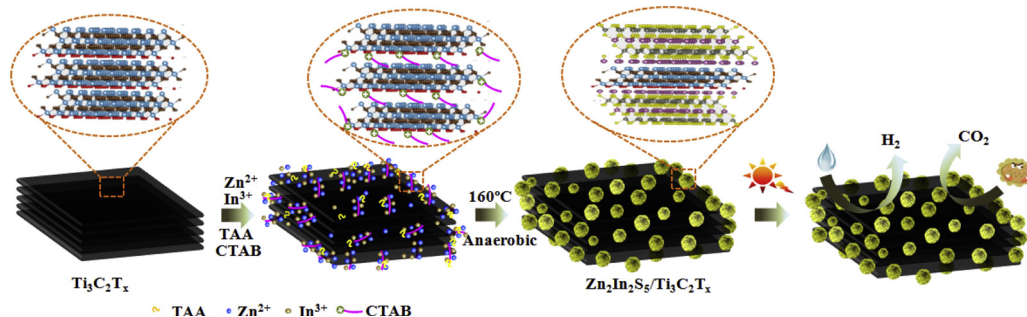


Fig. 1. Schematic illustration of the synthesis process of $\text{Zn}_2\text{In}_2\text{S}_5/\text{Ti}_3\text{C}_2(\text{O}, \text{OH})_x$ hybrids for hydrogen generation from water splitting and pollutant elimination.

manipulation at the atomic level becomes a feasible way to control the transfer and separation of photoexcited carriers. Xie et al. reported that the substitution of oxygen with the lattice sulfur atoms of ZnIn_2S_4 increased the density of states at valence-band maximum compared with that of the pristine ZnIn_2S_4 , which can provide more charge carriers for photocatalysis [16]. They also concluded that the zinc vacancies of ZnIn_2S_4 with higher charge density could enhance the carrier transport (15 ps) from the conduction band (CB) to the trap states, markedly promoting the separation efficacy of charge carriers (1.7 times) and thereby photoabsorption [17]. Zhang et al. found that the MoS_2 quantum dots induced by sulfur vacancy in ZnIn_2S_4 could act as electron traps, control charge flow (preventing vertical transmission of electrons), and enrich electrons onto the Zn facet [18].

In the $\text{Zn}_m\text{In}_2\text{S}_{3+m}$ system, increasing the layers of S-Zn-S could also change the band structure with available photons used and controllable redox potential. When the value of m increase from 1 to 5, the band gap is increased from 2.46 to 2.86 eV [13,19]. Preliminary investigations indicated that $\text{Zn}_2\text{In}_2\text{S}_5$ had the most suitable conduction band level and band gap for photoexcitation kinetics [13,20]. Poulios et al. and Song et al. demonstrated that the n-type $\text{Zn}_3\text{In}_2\text{S}_6$ had beneficial photoelectrochemical behavior and color-adjustable luminophores related to the recombination and transition of donor-acceptor pairs in shallow and intrinsic trap states [21,22]. Our group also developed a hierarchical 2D-2D $\text{Zn}_3\text{In}_2\text{S}_6/\text{FPCN}$ (fluorine doped carbon nitride) photocatalyst with enhanced activity for photocatalytic degradation and hydrogen generation in comparison to the pure $\text{Zn}_3\text{In}_2\text{S}_6$ or FPCN [23]. In terms of enhancing photocatalytic performance of single ternary chalcogenides ($\text{Zn}_2\text{In}_2\text{S}_5$, ZIS), heterogeneous coupling with metallic compound is a promising strategy.

MXene, a family of transition metal carbides/carbonitrides/nitrides, has revealed outstanding prospects in electrochemical electrode, catalyst, membrane separator, adsorbent, sensor and cellular imaging due to the metallic conductivity, tunable surface-terminated chemistry, charge mobility anisotropy and layer-dependent optics [24–31]. Take the $\text{Ti}_3\text{C}_2\text{T}_x$ ($\text{T}_x = -\text{F}$, $-\text{OH}$, or $-\text{O}$) for example, the electrical conductivity is $4600 \pm 1100 \text{ S cm}^{-1}$ with highly anisotropic carrier mobility, favoring the capture and transfer of photogenerated electron–hole pairs in photocatalysis [32]. Abundant exposed metal sites (or deficiency) facilitate the catalytic hydrogen evolution, CO_2 reduction and N_2 fixation reactions [33]. In addition, the surface adjustable chemistries with different terminated groups do not only control the Gibbs free energy ($|\Delta G_{\text{H}^+}|$) of intermediate adsorbed H^+ from the thermodynamics viewpoint, but also provide a strong interfacial contact between cocatalyst and photocatalyst [34]. Therefore, coupling active photocatalyst with $\text{Ti}_3\text{C}_2\text{T}_x$, such as $\text{Ti}_3\text{C}_2\text{T}_x/\text{CdS}$ [34,35], $\text{Ti}_3\text{C}_2\text{T}_x/\text{C}_3\text{N}_4$ [36–38], $\text{Ti}_3\text{C}_2/\text{Bi}_2\text{WO}_6$ [39], $\text{Ti}_3\text{C}_2/\text{Ag}_3\text{PO}_4$ [40] and $\text{Ti}_3\text{C}_2/\text{TiO}_2$ [41–43], becomes a favorable and popular way to boost the photocatalytic efficiency. Among these, Xie et al. demonstrated that $\text{Ti}_3\text{C}_2\text{T}_x$ was a Janus cocatalyst for both boosting the electron extraction from CdS for photocatalytic 4-nitrophenol reduction and inhibiting photocorrosion of CdS via the Cd^{2+} confinement effect [35]. In addition to the superior electrical conductivity and charge-carrier

separation ability of Ti_3C_2 , Ye et al. reported that the surface-alkalized Ti_3C_2 could enhance the CO_2 adsorption and activation sites for improving the CO_2 reduction rate [42]. Through constructing a heterojunction between ultrathin Ti_3C_2 and Bi_2WO_6 nanosheets, Gao et al. found that the hybrids showed enhanced CH_4 and CH_3OH yields from photocatalytic CO_2 reduction because of the short interfacial charge transport distance with large interfacial contact area [39]. However, there exists a gap in understanding with respect to the heterostructured coupling interaction for the improvement of photocatalytic activity of $\text{Ti}_3\text{C}_2\text{T}_x$ -based hybrids photocatalyst. Does the metal-to-metal charge transfer exist between metal atoms of photoactive semiconductor and the exposed Ti atoms of $\text{Ti}_3\text{C}_2\text{T}_x$ (MX) to change the spin states of metal sites and the coupling interactions, further affecting the symmetry in charge distribution? Also, no study on the synthesis of the $\text{Zn}_2\text{In}_2\text{S}_5/\text{Ti}_3\text{C}_2(\text{O}, \text{OH})_x$ (ZIS-MX) hybrid photocatalyst for hydrogen production and environmental pollutant elimination has been reported to date.

In this study, the $\text{Ti}_3\text{C}_2(\text{O}, \text{OH})_x$ was adopted as a 2D platform to grow *in situ* hierarchically flower-like $\text{Zn}_2\text{In}_2\text{S}_5$ microsphere by a facile hydrothermal method under anaerobic condition (Fig. 1). Various techniques were adopted to characterize the morphology and crystal structure, chemical state and photo-electrochemical properties. Density functional theory calculations have been used to resolve the heterostructured coupling interaction (especially in the metal-to-metal charge transfer) between $\text{Zn}_2\text{In}_2\text{S}_5$ and $\text{Ti}_3\text{C}_2(\text{O}, \text{OH})_x$. Experimental results indicate that the hybrids have superior visible-light-photocatalytic performance towards hydrogen production and environmental pollutant elimination. The mechanism underlying the enhanced photocatalytic performance was that the interfacial-built-in quasi-alloying effect drove electrically and spatially photoexcited charge separation in hierarchical $\text{Zn}_2\text{In}_2\text{S}_5/\text{Ti}_3\text{C}_2(\text{O}, \text{OH})_x$ hybrids.

2. Results and discussion

2.1. Synthesis and characterization of hierarchical photocatalyst

The X-ray diffraction (XRD) patterns of $\text{Ti}_3\text{C}_2\text{T}_x$, ZIS and the ZIS-MX composite are presented in Fig. 2a. The diffraction peaks at 9.1° , 18.4° , 27.7° , 34.6° and 60.8° corresponds to the reflection of $\text{Ti}_3\text{C}_2\text{T}_x$ [44,45]. The XRD patterns of ZIS and all the ZIS-MX composites present similar profiles, which are indexed to a hexagonal phase. The peaks located at $2\theta = 21.3^\circ$, 27.9° , 28.9° , 47.5° and 56.5° are distinctly indexed respectively to the (006), (102), (104), (112), and (202) crystal planes of the hexagonal $\text{Zn}_2\text{In}_2\text{S}_5$ phase structure. As shown in the ball-and-stick model in Fig. 2a, the $\text{Zn}_2\text{In}_2\text{S}_5$ phases include two layers of $-\text{S}\text{Zn}\text{S}-$ and a circular structural unit ($-\text{SIn}(o)\text{SIn}(t)\text{SAS}-$) with indium layers in octahedral (o) and tetrahedral (t) sites. [13] The vacant (Δ) sites have also been demonstrated by the electron spin resonance (ESR) with the g -value of 2.00, as shown in Fig. 2b. However, the disappearance of the peak corresponding to $\text{Ti}_3\text{C}_2(\text{O}, \text{OH})_x$ is ascribed to the low loading (0.7 wt% ~ 6.0 wt%) and good distribution of $\text{Ti}_3\text{C}_2(\text{O}, \text{OH})_x$ in contrast to $\text{Zn}_2\text{In}_2\text{S}_5$. Similar results have been shown by Cao et al and Ran et al. [39,46]

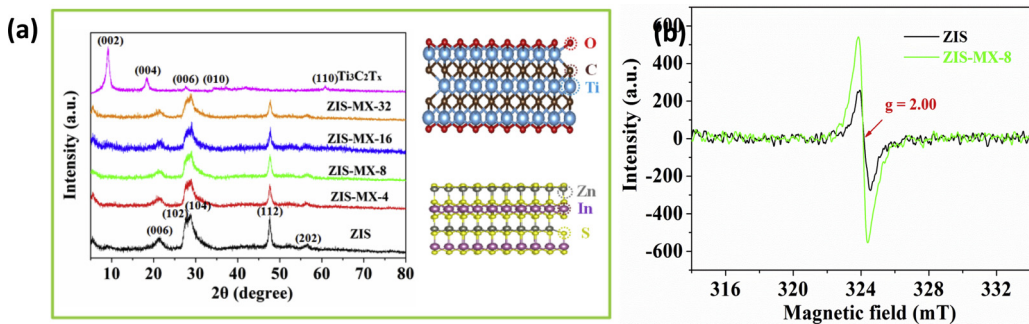


Fig. 2. (a) XRD patterns of as-obtained photocatalysts and (b) ESR spectra of ZIS and ZIS-MX-8.

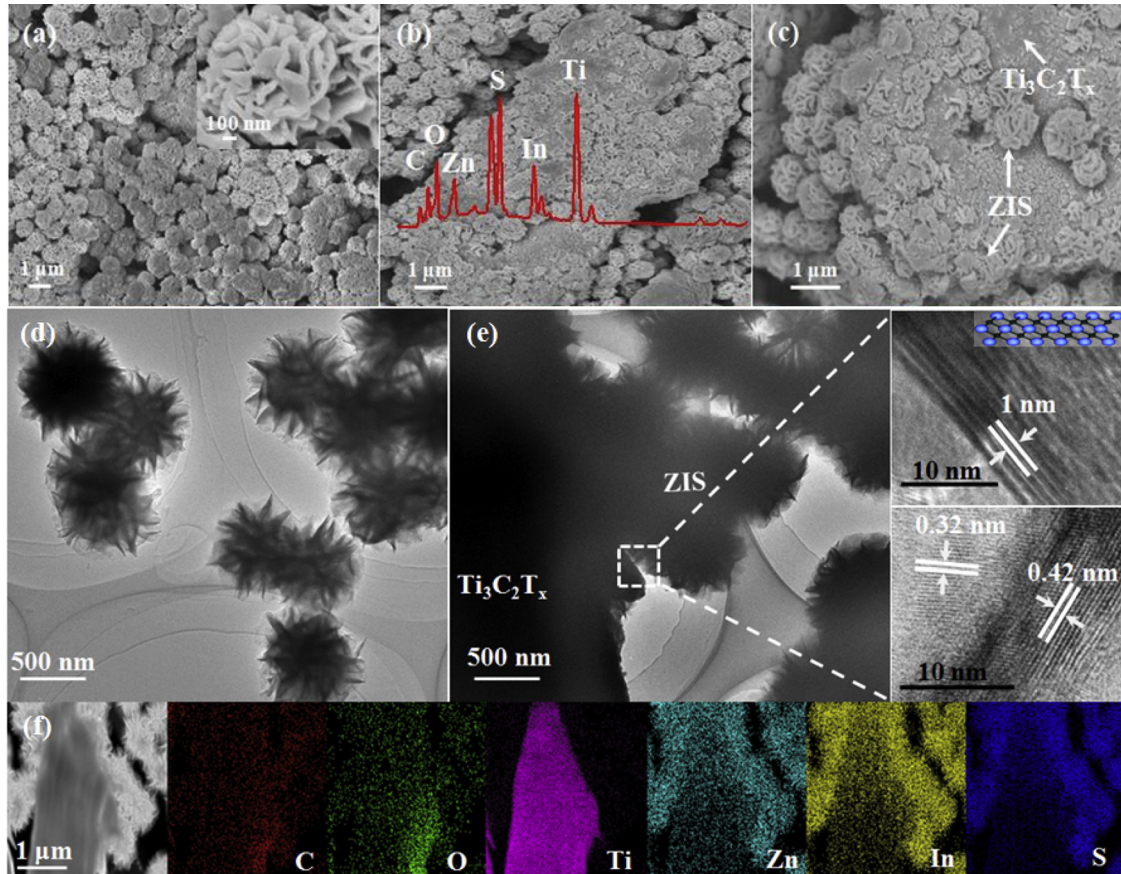


Fig. 3. FESEM images of (a) pure Zn₂In₂S₅, (b,c) Zn₂In₂S₅/Ti₃C₂(O, OH)_x hybrids (overlay with the SEM-EDX spectra); STEM images of (d) pure Zn₂In₂S₅ and (e) Zn₂In₂S₅/Ti₃C₂(O, OH)_x hybrids; (f) element mapping of the Zn₂In₂S₅/Ti₃C₂(O, OH)_x hybrids in HAADF-STEM.

The microstructure and morphology of ZIS and ZIS-MX composite were studied via field emission scanning electron microscopy (FESEM) and spherical aberration corrected transmission electron microscopy (STEM). Pristine Zn₂In₂S₅ (shown in Fig. 3a) exhibited uniformly flower-like microspheres with numerous petals/sheets. The diameter of each microsphere was less than 1 μm and the thickness of petals/sheets was \sim 60 nm. Fig. S1 indicates that the Ti₃C₂T_x exhibited a layered morphology with interconnected structure, providing plentiful open channels for ions transport and diffusion. Because the negatively charged Ti₃C₂T_x with the zeta potential of -28.6 mV had hydrophilic surfaces and different kinds of functional groups (i.e., $-\text{OH}$, $-\text{O}$ or $-\text{F}$), [28,30] the layered Ti₃C₂T_x can immobilize the In³⁺ and Zn²⁺ cations in aqueous solution (Fig. 1). Notably, cetyltrimethylammonium bromide (CTAB) not only served as the prepillar agent to increase the interlayer spacing of Ti₃C₂T_x for In³⁺ and Zn²⁺ cations intercalation by ion-exchange interaction, but also as the surfactant for effectively

controlling the uniform growth of ZIS and impeding the agglomeration of particles. [47] Favorable activation energy in the interior of Ti₃C₂T_x has been reported to drive the metal ions adsorption and intercalation near the edges of Ti₃C₂T_x or the diffusion to the deeper sites. [30,48] The S²⁻ anions from thioacetamide reacted with the adsorbed In³⁺ and Zn²⁺, causing the *in situ* heterogeneous nucleation and growth of the Zn₂In₂S₅ microsphere. FESEM images (Fig. 3b and 3c) of ZIS-MX-8 (8 mg Ti₃C₂T_x was added during the synthesis process) indicate the intimate contact between the ZIS micro-marigold and Ti₃C₂(O, OH)_x. Energy Dispersive X-Ray (EDX) analysis (Fig. 3b) reveals only the existence of C, Ti, Zn, In, S and O, which proves no impurities in composites. Evidently, the $-\text{F}$ terminations of Ti₃C₂T_x may be replaced by $-\text{O}$ and $-\text{OH}$ to give Ti₃C₂(O, OH)_x in the oxygen-deficient hydrothermal environment.

The STEM image (Fig. 3d) further verifies the uniform flower-like Zn₂In₂S₅ microsphere (\sim 600 nm) with ultrathin sheets. Fig. 3e shows

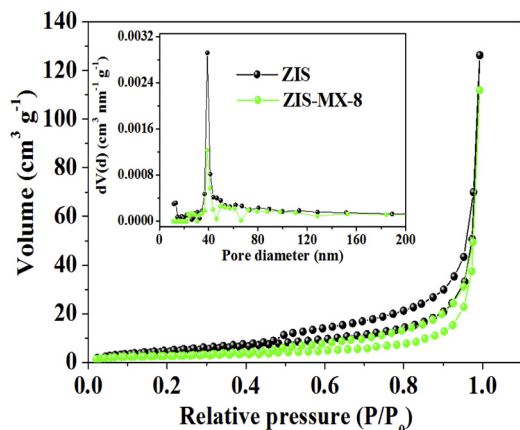


Fig. 4. N_2 adsorption – desorption isotherms of pure ZIS and ZIS-MX-8 hybrids; the inset is the corresponding pore size distribution.

that ZIS was grown on the surface of bulk $\text{Ti}_3\text{C}_2(\text{O}, \text{OH})_x$. High-resolution TEM reveals the heterojunction formation of $\text{Ti}_3\text{C}_2(\text{O}, \text{OH})_x$ and ZIS crystals with well-defined lattice fringes, as reflected in the lighter-shade regular stripes with an interlayer spacing of 1 nm, corresponding to the (002) plane of $\text{Ti}_3\text{C}_2(\text{O}, \text{OH})_x$. Two kinds of stripes with inter-planar distances of 0.32 nm and 0.42 nm were observed, corresponding respectively to the (104) and (006) planes of ZIS. The element mapping (Fig. 3f) of the ZIS/MX composites in high angle annular dark field scanning transmission electron microscopy (HAADF-STEM) indicate the existence of C, O, Ti, Zn, In and S elements which were homogeneously distributed throughout the particles. Obviously, compared with the Ti, O and C elements, the greater densities of Zn, S and In elements on the external surface of $\text{Ti}_3\text{C}_2(\text{O}, \text{OH})_x$ imply that the $\text{Ti}_3\text{C}_2(\text{O}, \text{OH})_x$ was wrapped by ZIS to generate the quasi-core-shell structure. These results suggest that the ZIS-MX composites have been successfully synthesized.

From the N_2 adsorption–desorption isotherms shown in Fig. 4, both pure ZIS and ZIS-MX-8 hybrids exhibited mesoporous characteristic (a type IV isotherm with the H3 hysteresis loop). Our previous research has demonstrated that pure $\text{Ti}_3\text{C}_2\text{T}_x$ had a surface area of $5.15 \text{ m}^2 \text{ g}^{-1}$ and pore volume of $0.024 \text{ cm}^3 \text{ g}^{-1}$ [45]. The specific surface area and pore volume of ZIS-MX-8 were $10.31 \text{ m}^2 \text{ g}^{-1}$ and $0.173 \text{ cm}^3 \text{ g}^{-1}$, respectively, which are lower than that of pure ZIS ($16.56 \text{ m}^2 \text{ g}^{-1}$ and $0.195 \text{ cm}^3 \text{ g}^{-1}$, respectively).

To better understand the interaction between ZIS and $\text{Ti}_3\text{C}_2(\text{O}, \text{OH})_x$, the coupling interaction were characterized by fine-scan X-ray photoelectron spectroscopy (XPS) measurements. In Fig. S2a, the peaks of the F element in ZIS-MX-8 disappeared, demonstrating the F element of $\text{Ti}_3\text{C}_2\text{T}_x$ was removed. The Zn/In/S molar ratios of ZIS and ZIS-MX-8 were similar at 1:0.8:2.2, revealing the formation of $\text{Zn}_2\text{In}_2\text{S}_5$ formula in both the pure component and composites. In the C 1 s pattern of ZIS-MX-8 (Fig. 5a), three peaks at 286.0, 284.2 and 281.6 eV are ascribed to C–O, C–Ti–O and Ti–C bonds, respectively, proving that the main $\text{Ti}_3\text{C}_2(\text{O}, \text{OH})_x$ structure is still retained [45]. Fig. 5b shows the In 3d_{3/2} (452.59 eV) and In 3d_{5/2} (445.04 eV), validating the existence of In(III) [49]. However, the binding energies shifted to 452.39 eV and 444.84 eV in the presence of $\text{Ti}_3\text{C}_2(\text{O}, \text{OH})_x$. The negative binding energy shifts suggest the additional coulombic interactions between the emitted electron and the indium core. The Zn 2p spectrum (Fig. 5c) centered at 1022.1 eV and 1045.13 eV, belongs to the Zn 2p_{3/2} and Zn 2p_{1/2}, respectively. A similar negative shift in hybrids has also been shown. Furthermore, in regard to the O 1 s spectra of $\text{Ti}_3\text{C}_2\text{T}_x$ (Fig. 5d), three peaks at 528.34, 530.15 and 531.31 eV correspond to the surface-adsorbed O species, Ti–O–Ti and Ti–OH, respectively [50]. After the immobilization of ZIS, the binding energies shifted to 529.94, 531.07 and 532.21 eV, which have higher binding energy compared to that in $\text{Ti}_3\text{C}_2\text{T}_x$. Similar shifts to higher binding energy were also observed in

the Ti 3d spectra (Fig. S2b), whereas the S 2p spectrum showed no change before and after the hybridization with $\text{Ti}_3\text{C}_2\text{T}_x$ (Fig. S2c). These results suggest strong interaction between the p-orbital (or s-orbital) of Ti atoms (or O atoms) and the unoccupied d-orbitals (or p-orbitals) of In atoms (or Zn atoms). It also infers that there was metal-to-metal charge transfer between metal atoms of $\text{Zn}_2\text{In}_2\text{S}_5$ and the exposed Ti atoms of $\text{Ti}_3\text{C}_2(\text{O}, \text{OH})_x$ to affect the spin states of metal sites and surface charge distribution. The strong interfacial coupling interaction at the atomistic level not only conferred interfacial-built-in quasi-alloying effects between ZIS and $\text{Ti}_3\text{C}_2(\text{O}, \text{OH})_x$, but also made for a reliable photochemical platform for favorable photoinduced charge transfer pathways [51,52]. This interfacial quasi-alloy is similar to the PdAu quasi-random, dendrimer-encapsulated nanoparticle alloys [53].

Ultraviolet-visible diffuse reflectance spectra (UV-vis DRS) were employed to measure the light-harvesting capability of the photocatalysts. In Fig. 5e, the $\text{Ti}_3\text{C}_2\text{T}_x$ had no distinct absorption edge in the range of 310–800 nm, testifying the metallic nature of $\text{Ti}_3\text{C}_2\text{T}_x$ [30]. To further ascertain the metallic characteristic of $\text{Ti}_3\text{C}_2\text{T}_x$, current-voltage measurements were carried out. As shown in Fig. 5f, the current had a good linear relationship with voltage for the prepared $\text{Ti}_3\text{C}_2\text{T}_x$ film, certifying metallic property and superior electrical conductivity of the obtained $\text{Ti}_3\text{C}_2\text{T}_x$ [54]. For ZIS, there was an intense absorption band with a steep edge around the wavelength of 453 nm in the visible-light region. The intense absorption of ZIS originated from the transition between the valence band ($\text{Zn}3\text{d} + \text{S}3\text{p}$) and the conduction band ($\text{In}5\text{s}5\text{p} + \text{Zn}4\text{s}4\text{p}$), but not the transition between the impurity level to the conduction band (CB) [13,55]. The presence of black $\text{Ti}_3\text{C}_2(\text{O}, \text{OH})_x$ merely increased the absorption baseline associated with the distinct adsorption of carbonaceous materials [41]. There was no change in the absorption edges and the band gaps of the composites, which indicates that light absorption was a negligible factor in the resulting photocatalytic performance of the ZIS-MX composites.

2.2. Photochemically reactive performance of photocatalyst

Photocatalytic oxidation performance can be typically assessed by the degradation of stable and persistent antibiotics (e.g., tetracycline hydrochloride, TC) using visible light. In Fig. 6a, negligible changes for TC concentration were shown in the blank experiments (without catalyst or no light), demonstrating the auto-degradation should be negligible throughout the 60 min duration investigated. Compared with pure ZIS (78.1%), all ZIS-MX hybrids owned higher photocatalytic TC degradation efficiency. The ZIS-MX-8 had the highest TC removal efficiency of 84.3%. Total organic carbon removal efficiency was 38.8%, suggesting a gradual mineralization of the organic pollutant. The photocatalytic degradation rate was evaluated via the pseudo-first order model ($\ln(C/C_0) = kt$, whereby k is the rate constant. As shown in Fig. 6b, the TC degradation rate was the fastest for ZIS-MX-8 (0.03043 min^{-1}), followed by ZIS-MX-16, ZIS-MX-32, ZIS-MX-4 and lastly ZIS. Notably, the visible-light photocatalytic TC degradation efficiency of ZIS-MX-8 was 1.25 fold higher than that of pure ZIS. Such performance enhancements are ascribed to the formation of strong coupling interactions between $\text{Ti}_3\text{C}_2(\text{O}, \text{OH})_x$ and ZIS that conferred two key advantages: (i) the photo-generated electrons from the CB of ZIS can effectively transfer across the interface of the composites and store on the surface of $\text{Ti}_3\text{C}_2(\text{O}, \text{OH})_x$ via interfacial-built-in quasi-alloying effect; and (ii) the unique photothermal conversion of $\text{Ti}_3\text{C}_2(\text{O}, \text{OH})_x$ affords energy to activate catalyst and accelerates the local photocatalytic reactions. To demonstrate the effect of reaction temperature, various temperatures of 35 °C, 45 °C and 55 °C were investigated. Fig. 6c indicates that the photocatalytic TC removal performance was improved with the increase of temperature, which is due to the enhanced mass transfer at the macroscopic level and also enhanced local heat at the microcosmic level that promoted the local surface catalytic reaction because of the photothermal conversion characteristics of $\text{Ti}_3\text{C}_2(\text{O}, \text{OH})_x$ [56]. A thermal imaging device was used to characterize the

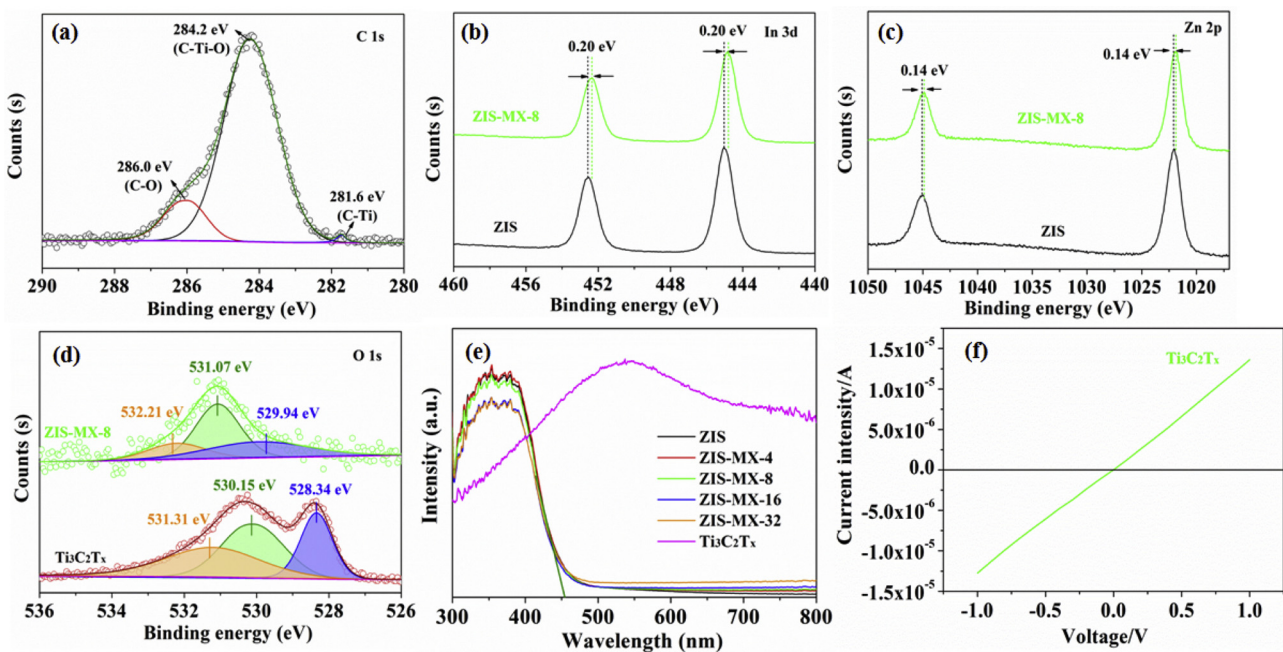


Fig. 5. XPS spectra of ZIS-MX-8: (a) C 1s, (b) In 3d, (c) Zn 2p and (d) O 1s. For comparison, the In 3d and Zn 2p spectra of ZIS and the O 1s spectra of $\text{Ti}_3\text{C}_2\text{T}_x$ are also shown; (e) UV–vis DRS spectrum, and (f) current–voltage curve for the $\text{Ti}_3\text{C}_2\text{T}_x$ film.

changes of surface temperature of the pristine $\text{Ti}_3\text{C}_2(\text{O}, \text{OH})_x$, ZIS and ZIS-MX composites (Fig. 7). Specifically, the average temperature of the ZIS-MX composite and $\text{Ti}_3\text{C}_2(\text{O}, \text{OH})_x$ surfaces increased by 5.0 °C and 18.1 °C, respectively, after 60 s of irradiation by the light-emitting diode light source (50 W). This demonstrates the photothermal conversion ability of $\text{Ti}_3\text{C}_2(\text{O}, \text{OH})_x$, which may partly contribute to the enhancement of the photocatalytic TC removal performance. Similar photothermal contribution to improve photocatalytic performance has also been reported by Gan et al. [57].

Hydrogen evolution from water splitting experiments were carried out to further evaluate the visible-light photocatalytic reduction activity of the as-prepared photocatalysts. Fig. 8a shows that the cumulative H_2 increased with time, with that for the ZIS-MX-8 composite increasing the fastest. All of the ZIS-MX composites showed improved photocatalytic hydrogen generation as compared to the pure ZIS, whose photocatalytic H_2 production performance was $6581.8 \mu\text{mol g}^{-1}$. The photocatalytic performance of ZIS was significantly enhanced upon coupling with $\text{Ti}_3\text{C}_2(\text{O}, \text{OH})_x$, as evident in the increase in the H_2 production by the ZIS-MX composites with increasing $\text{Ti}_3\text{C}_2(\text{O}, \text{OH})_x$ content, achieving a maximum of $12,983.8 \mu\text{mol g}^{-1}$ at the mass ratio of 1.5%, which is about 1.97 times higher than that of pure ZIS. The

improvement is due to the construction of the ZIS/ $\text{Ti}_3\text{C}_2(\text{O}, \text{OH})_x$ heterojunction that effectively boosted the photocatalytic H_2 -production activity via the synergistic effect of photoactive ZIS and metallic $\text{Ti}_3\text{C}_2(\text{O}, \text{OH})_x$. Fig. 8b further quantifies the average H_2 production rates of the as-obtained samples as 1316.4 and $2596.8 \mu\text{mol h}^{-1} \text{g}^{-1}$ for ZIS and ZIS-MX-8, respectively. The H_2 generation rate of ZIS-MX-8 is comparable to that of other works reported recently (Table S1). Moreover, ZIS-MX-8 exhibited an apparent quantum efficiency of 8.96% at 420 nm. Notably, a further increase in the content of $\text{Ti}_3\text{C}_2\text{T}_x$ from 1.5% to 6.0% resulted in a decrease in photocatalytic H_2 production. ZIS-MX-32 exhibited the lowest photocatalytic H_2 production activity of $1585.7 \mu\text{mol h}^{-1} \text{g}^{-1}$ because of the blocked active sites and shielded light absorption by the redundant $\text{Ti}_3\text{C}_2(\text{O}, \text{OH})_x$. Therefore, the $\text{Ti}_3\text{C}_2(\text{O}, \text{OH})_x$ amount has to be optimized to achieve the optimal H_2 production by the ZIS-MX composites.

The recovery and reuse of photocatalysts is also a significant factor for the practical implementation. Accordingly, the recyclability of ZIS-MX-8 was investigated by repeated photocatalytic H_2 generation over six cycles under the same conditions. Fig. 8c shows that ZIS-MX-8 still retained 67.6% of its original photocatalytic activity after six cycles, indicating reasonable photocatalytic stability. In addition, the XRD and

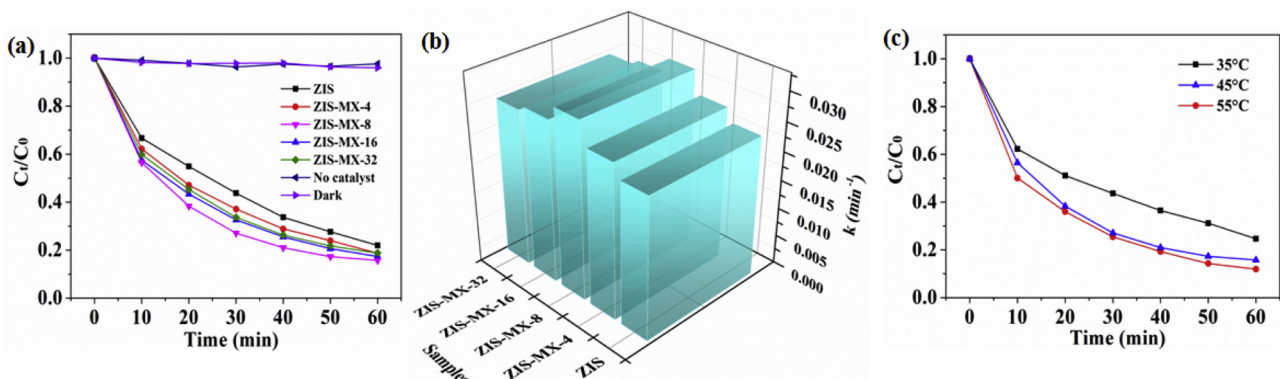


Fig. 6. Photocatalytic degradation of TC: (a) evolution of degradation with time; (b) pseudo-first order rate constants for pure ZIS and ZIS-MX hybrids; and (c) photocatalytic degradation of TC by ZIS-MX-8 at different reaction temperatures.

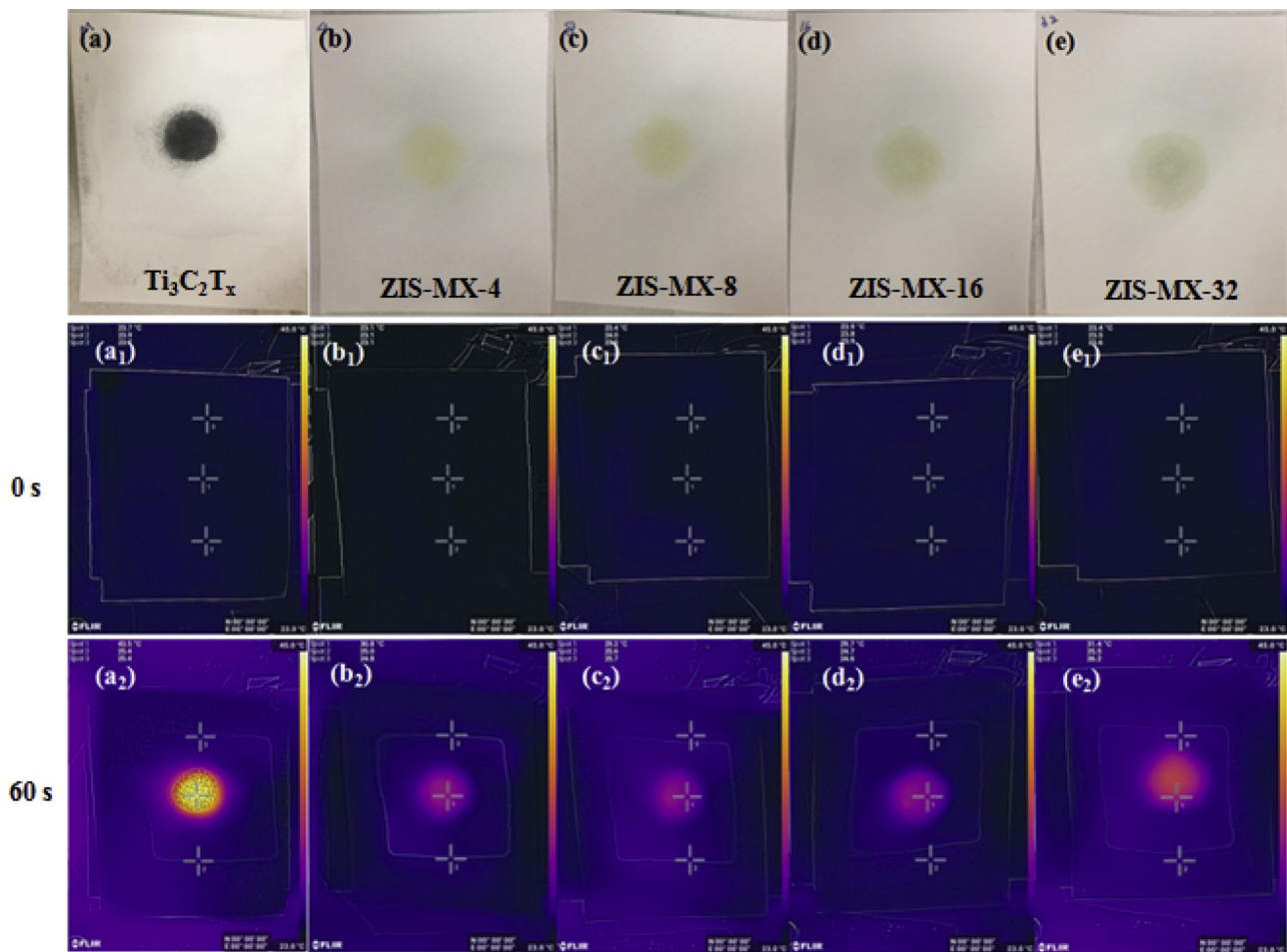


Fig. 7. Surface temperature change of pristine $\text{Ti}_3\text{C}_2\text{T}_x$ and ZIS-MX hybrids before (a₁–e₁) and after (a₂–e₂) the light illumination. In addition, the originally pristine $\text{Ti}_3\text{C}_2\text{T}_x$ and ZIS-MX hybrids (a–e) have also been added for comparison.

SEM of the ZIS-MX-8 before and after the six cycles of photocatalytic reaction was also acquired. No obvious differences in the XRD patterns (Fig. 9a) and morphology (Fig. 9b and c) are observed, demonstrating a stable crystal structure after repeated uses. The activity decay may be mainly because of the fouling of active sites by the byproducts and the decreased concentration of sacrificial reagent. The above analysis indicates that the ZIS-MX-8 presented both excellent photocatalytic activity and structural stability.

2.3. Electrical promotion from experimental evidences and theoretical insights

To investigate the band structures/positions of ZIS, the density functional theory calculation, valence XPS and Mott–Schottky measurements were carried out. The calculated density of states (DOS) curves (Fig. 10a) indicate that the ZIS possessed typical semiconductor with a characteristic band gap of ~0.8 eV. The S3p orbitals significantly contributed to the top valence band of ZIS, the highest occupied molecular orbital (HOMO) levels were dependent on the hybridized S3p and Zn3d orbitals, while the hybridized In5s5p and S3p orbitals mainly

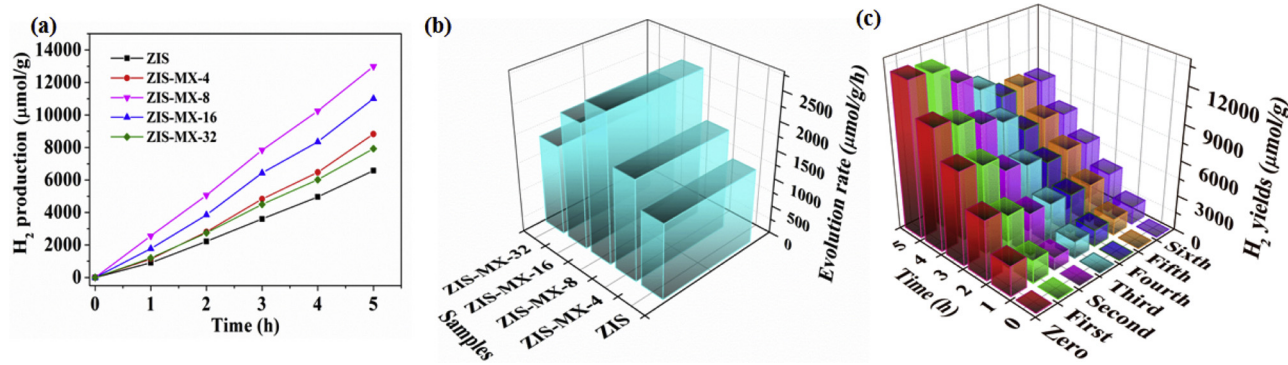


Fig. 8. Photocatalytic H_2 evolution: (a) cumulative amount of H_2 with time; (b) H_2 evolution rate; and (c) recyclability of ZIS-MX-8 for H_2 generation under visible light irradiation.

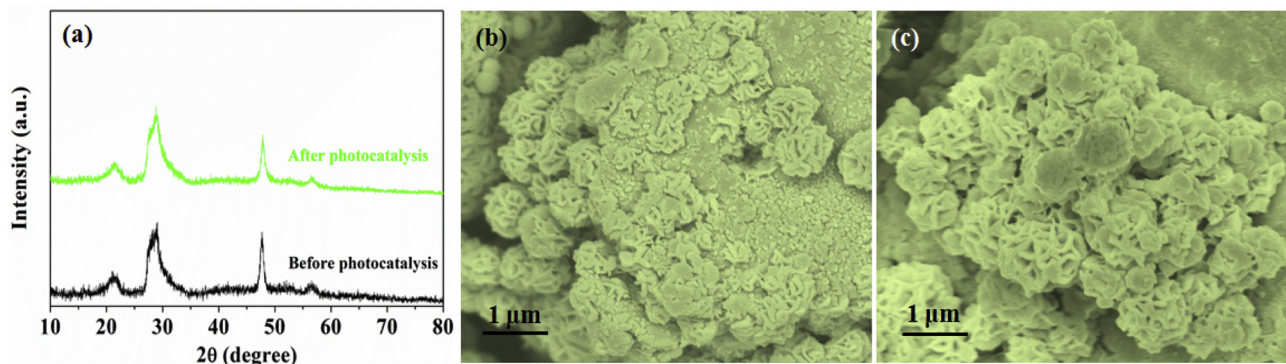


Fig. 9. Characterization of ZIS-MX-8 before and after photocatalytic H₂ generation: (a) XRD patterns; (b) SEM image before photocatalysis; and (b) SEM image after photocatalysis.

determined the lowest unoccupied molecular orbital (LUMO) levels. Fig. S3 further shows that the band gap energy (E_g) of pure ZIS based on the UV-vis DRS can be estimated to be 2.87 eV. Such an underestimation of band gap originated from the artifact of the generalized gradient approximation (GGA) method [14]. The energy gap of semiconductors from the valence band maximum (VBM) to the Fermi level (E_F) was experimentally studied via the valence XPS. From Fig. 10b, the VBM position of ZIS was 1.53 eV. Furthermore, the Mott–Schottky measurements (Fig. 10c) showed that the MS curves had a positive slope, indicating the n-type semiconductor characteristics of ZIS [58]. The flat band position of the ZIS is approximately −1.54 V versus Ag/AgCl at the measurement frequencies of 500 Hz and 1000 Hz. Generally, the conductor band potential of ZIS is near the flat band potential. So the CB potentials of ZIS can be converted to −1.34 eV (vs. NHE) [59]. With the known optical properties, the VB potential was calculated to be 1.53 eV, which is consistent with the results of the valence XPS.

To explore the electrical effect in the hybridized system, the steady-state photoluminescence (PL), transient-state time-resolved PL spectra and photoelectrochemical measurements have been conducted. As shown in Fig. 11a, the quenched photoluminescence emission peak of ZIS-MX-8 under the excitation wavelength of 325 nm was lower than that of pure ZIS, arising from the efficient charge dissociation and migration between ZIS and Ti₃C₂(O, OH)_x via interfacial-built-in quasi-alloying effect. Ground state electrons inside the ZIS are stimulated and transformed into the excited state once the photons are absorbed. After returning to the thermal equilibrium state for these excited electrons, the excess energy was released via the radiative and nonradiative decay processes [39]. The band edge emission of ZIS and ZIS-MX-8 decays via the electron-hole recombination can be well profiled by biexponential model (shown in the Section 2 of supporting information). As shown in Fig. 11b, ZIS-MX-8 had a markedly decreased short ($\tau_1 = 1.024$ ns, 86.5%), long ($\tau_2 = 3.018$ ns, 13.5%) and average ($\tau = 1.652$ ns

fluorescence lifetime vis-à-vis ZIS ($\tau_1 = 1.531$ ns, 96.7%; $\tau_2 = 5.920$ ns, 3.3%; average $\tau = 1.902$ ns). The fast and slow components are ascribed to decay from the free exciton states and the bound exciton states, respectively [60]. The decreased PL lifetime suggests the existence of more efficient non-radiative decay pathways in ZIS-MX-8 originated from the electron transfer from ZIS to Ti₃C₂(O, OH)_x with the aid of the interfacial-built-in quasi-alloying effect. Assuming that the difference in the exciton lifetimes was only due to the added electron-transfer process [60,61], the electron-transfer rate constants (k_{ET}) in ZIS-MX-8 was estimated to be 0.32×10^9 s^{−1}, using τ_1 values of ZIS and ZIS-MX-8, according to the following equation:

$$k_{ET} = \frac{1}{\tau_1(ZIS - MX - 8)} - \frac{1}{\tau_1(ZIS)}$$

Therefore, the electron-transfer efficiency (calculation in the Section 3 of supporting information) from ZIS to Ti₃C₂(O, OH)_x can then be calculated to be 33.0%. From the photoluminescence results, the recombination of photo-induced charge carriers has been effectively suppressed caused by the efficient interfacial charge transfer upon the strong interaction of ZIS and Ti₃C₂(O, OH)_x.

Surface charge recombination rate was evaluated using the decay profile of the open-circuit potential (Voc). The average recombination rate can be assessed using the following equation:

$$\frac{E - E_{light}}{E_{dark} - E_{light}} = 1 - \exp(-kt)$$

where E, E_{dark}, and E_{light} are the open-circuit potential at any time, in dark and under light irradiation, respectively; and k is the pseudo-first-order recombination rate constant [58,62]. As evident in Fig. 11c, the ZIS-MX-8 (0.0104 s^{−1}) exhibited slower decay kinetics in comparison to ZIS (0.0152 s^{−1}) after the light was switched off, suggesting that surface recombination rate was dramatically suppressed.

Charge transfer was studied via electrochemical impedance

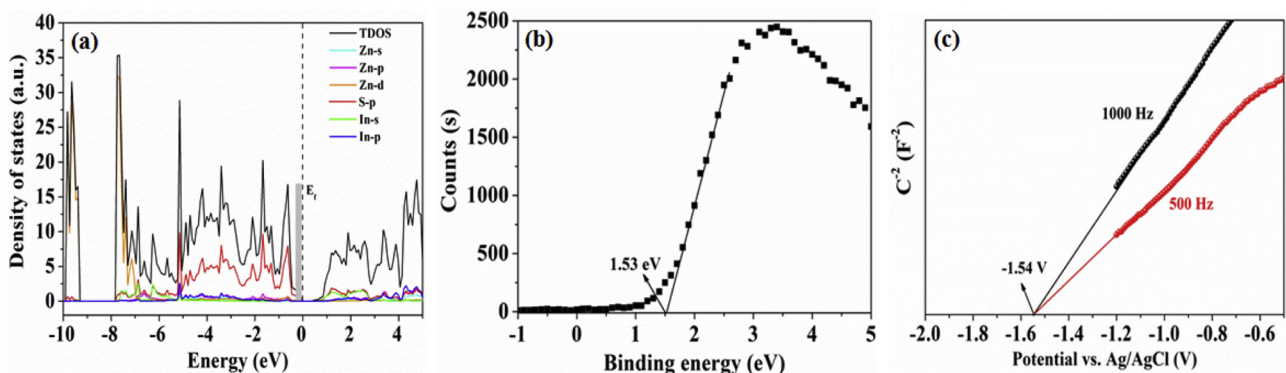


Fig. 10. The density of states (a), valence XPS spectra (b) and Mott–Schottky measurements (c) of ZIS.

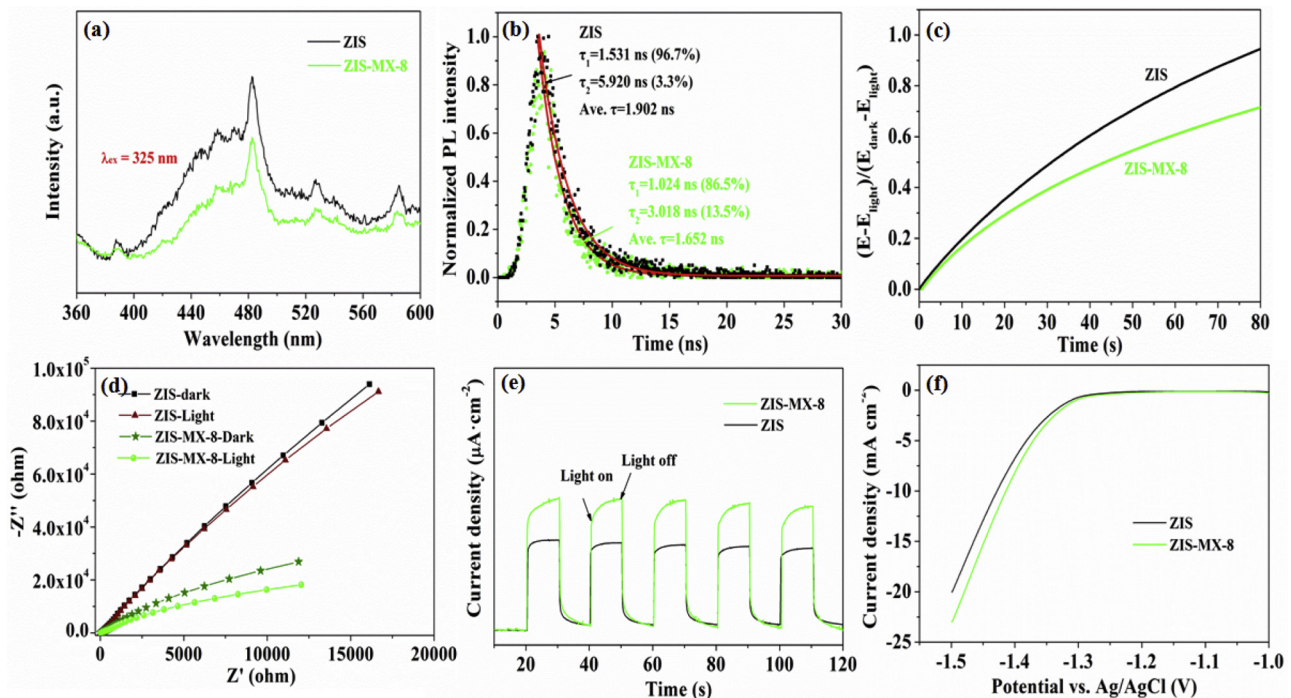


Fig. 11. Comparison of ZIS and ZIS-MX-8: (a) steady-state PL spectra; (b) time-resolved PL spectra; (c) normalized open-circuit potential decay curves; (d) transient photocurrent responses; (e) electrochemical impedance spectroscopy (EIS) changes; and (f) polarization curves.

spectroscopy and transient photocurrent. In Fig. 11d, only one arc radius can be obtained in the measured frequency ranges, implying that only the surface charge-transfer mode occurred during the photocatalytic process. The Nyquist plot of ZIS-MX-8 has a smaller arc radius in comparison to the ZIS, demonstrating the higher electronic conductivity of ZIS-MX-8 due to electron transfer between ZIS and $\text{Ti}_3\text{C}_2(\text{O}, \text{OH})_x$. The low charge transfer resistance/high electronic conductivity favored more efficient charge separation. Moreover, the arc radii of ZIS and ZIS-MX-8 decreased after the surfaces were exposed to visible light, indicating that the electronic conductivity of ZIS-MX-8 and ZIS decreased. Transient photocurrent responses of ZIS and ZIS-MX-8 were obtained under intermittent visible light irradiation for five periodic on-off cycles at a constant bias of 0.5 V vs. Ag/AgCl reference electrode with the measured solution pH of 6.8, as displayed in Fig. 11e. Consistently over multiple cycles, the photocurrent intensities increased instantaneously once the light was on, and the signals sharply declined when the light is turned off. Clearly, the photocurrent density of ZIS-MX-8 was higher than that of ZIS, because the enhanced electron-hole separation and charge carrier transfer via the “bridge” function of quasi-alloying effect made the photo-induced charge more favorable in the photocatalytic redox reaction. [63] Taking the reduction reaction for example, Fig. 11f shows the polarization curve of the ZIS-MX-8/FTO (fluorine-doped tin oxide glass) electrode together with that of ZIS/FTO as a control. The cathodic current observed in the potential range from -1.0 to -1.5 V vs Ag/AgCl corresponds to the reduction of water to H_2 . In comparison with the ZIS/FTO electrode in the I-V curve, the ZIS-MX-8/FTO electrode shows much enhanced cathodic current. This lower over-potential of ZIS-MX-8 might be due to the fast interfacial electron transfer at the ZIS and $\text{Ti}_3\text{C}_2(\text{O}, \text{OH})_x$ interface, further confirming that the $\text{Ti}_3\text{C}_2(\text{O}, \text{OH})_x$ is a good cocatalyst that can efficiently enhance the photocatalytic activity.

To provide a quantitative and visual understanding in interfacial-built-in quasi-alloying effect between ZIS and $\text{Ti}_3\text{C}_2(\text{O}, \text{OH})_x$, density functional theory (DFT) + U calculations were used to theoretically elucidate the electronic structure of ZIS and $\text{Ti}_3\text{C}_2(\text{O}, \text{OH})_x$ individual, as well as their composites. The calculated density of states curve (Fig. 10a and Fig. 12a) shows that ZIS has semiconductor characteristics while

the $\text{Ti}_3\text{C}_2(\text{O}, \text{OH})_x$ has metallic characteristics. The near-Fermi bands of $\text{Ti}_3\text{C}_2(\text{O}, \text{OH})_x$ are represented mainly by finite Ti 3d orbitals. For a stable ZIS/ $\text{Ti}_3\text{C}_2(\text{O}, \text{OH})_x$ Schottky interface (Fig. 12b), the electronic structure of both ZIS and $\text{Ti}_3\text{C}_2(\text{O}, \text{OH})_x$ exhibit a significant change in In 5s5p, S3p and Ti 3d orbitals, as a result of the strong donor-acceptor coupling at their interface, which is in accordance with XPS results (Fig. 5b-d and Fig S2). The Fermi level on ZIS and $\text{Ti}_3\text{C}_2(\text{O}, \text{OH})_x$ were calculated to be -4.11 eV and -0.10 eV, respectively, suggesting the charges would flow from $\text{Ti}_3\text{C}_2(\text{O}, \text{OH})_x$ to ZIS once contacted. The work function (Φ) of ZIS and $\text{Ti}_3\text{C}_2(\text{O}, \text{OH})_x$ were calculated to be 6.81 and 5.92 eV (Fig. 12c-d), respectively, further confirming the direction of charge flow from $\text{Ti}_3\text{C}_2(\text{O}, \text{OH})_x$ to ZIS. Hence, the electrons would transfer from $\text{Ti}_3\text{C}_2(\text{O}, \text{OH})_x$ to ZIS in the hybridization process (Fig. S4), resulting in a decrease of electron concentration in $\text{Ti}_3\text{C}_2(\text{O}, \text{OH})_x$ and an increase in ZIS. Moreover, the electronegativities of In is 1.78, which is larger than that of Ti (1.54) and Zn (1.65), which indicates that the In atom tended to have stronger electron affinities with the Ti atom than with the Zn atom. This trend is also a reflection of the quasi-alloying effect at the interfacial structure between ZIS and $\text{Ti}_3\text{C}_2(\text{O}, \text{OH})_x$. A similar bonding phenomenon has been observed in the Cu atom bonding in the AgCu alloy [64]. The differential charge density in ZIS/ $\text{Ti}_3\text{C}_2(\text{O}, \text{OH})_x$ was further visualized in Fig. 12e. Apparently, the surface metal atoms of ZIS extracts electron density from the adjacent metal atom of $\text{Ti}_3\text{C}_2(\text{O}, \text{OH})_x$ at the interface. Based on the Bader charge analysis [65], the amount of transferred electron is about 1.27 electrons per unit cell via the interface of metal-to-metal. These electrical steering at the atomic level via the interfacial-built-in quasi-alloying effect generates an internal electric field that is advantageous for the separation of electron-hole pairs [66]. Once the electrons are excited from the S 2p orbital to the In 5s5p orbital in ZIS, they can rapidly be injected into the Ti 3d orbitals in $\text{Ti}_3\text{C}_2(\text{O}, \text{OH})_x$, leaving a longer-lived hole in ZIS and thereby more efficient spatial separation of electron and holes. Moreover, the quasi-alloying effect at the interface of ZIS and $\text{Ti}_3\text{C}_2(\text{O}, \text{OH})_x$ also favor a stronger bonding to the electronegative species (i.e. O_2) and a weaker bonding to the electropositive species (i.e. H_3O^+ and H^*) [64].

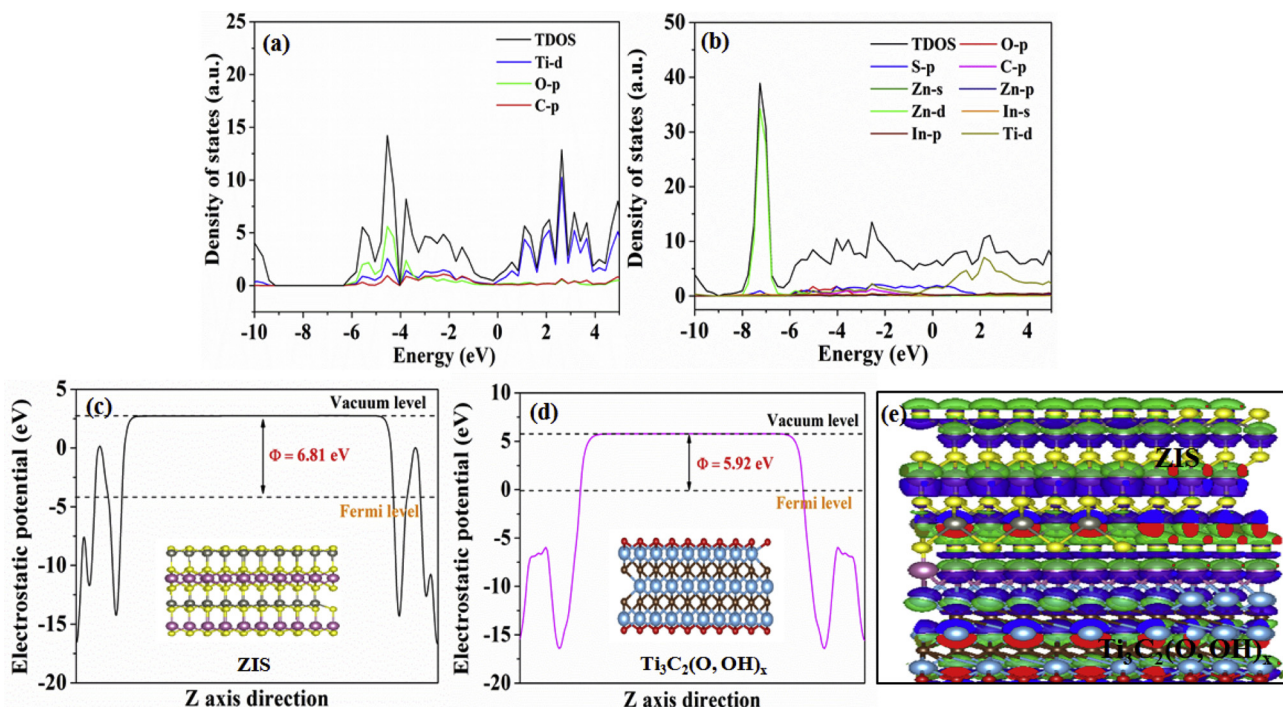


Fig. 12. The density of states for $\text{Ti}_3\text{C}_2(\text{O}, \text{OH})_x$ (a) and ZIS/ $\text{Ti}_3\text{C}_2(\text{O}, \text{OH})_x$ hybrids (b); The average potential profile along Z-axis direction for ZIS (c) and $\text{Ti}_3\text{C}_2(\text{O}, \text{OH})_x$ (d). The differential charge density (e) of ZIS/ $\text{Ti}_3\text{C}_2(\text{O}, \text{OH})_x$ hybrids. The differential charge density is defined as the difference in electronic density before and after bonding. The atoms in yellow, purple, silver, light blue, brown and red represent S, In, Zn, Ti, C and O, respectively. The isosurfaces were set to be $0.31 \text{ e}/\text{\AA}^3$, and the spheres in green and dark blue depict positive and negative charges, respectively (For interpretation of the references to colour in this figure legend, the reader is referred to the web version of this article).

2.4. Photocatalytic reaction mechanism

2.4.1. Organics oxidizing degradation

After the photogenerated carrier (electron or hole) transfer, a large amount of oxidative species (such as peroxide radicals, hydroxyl radicals or holes) in the photocatalytic pollutant degradation system can be produced after the redox reaction between the free electron or holes in reactive sites and the medium (like H_2O , dissolved O_2 and even organic species) [67,68]. In the dark, the dissolved O_2 molecules can be absorbed by unsaturated Ti 3d orbitals (i.e., bulk-defects such as Ti interstitials in the coordinated Ti atoms) in $\text{Ti}_3\text{C}_2(\text{O}, \text{OH})_x$ via the charge-donating defect effect and quasi-alloying effect [69,70]. As shown in Fig. 13, once exposed to visible light, the photogenerated electrons of ZIS was excited from the VB to the CB to produce the electron-hole pairs, accompanied by the migration from the CB of ZIS to $\text{Ti}_3\text{C}_2(\text{O}, \text{OH})_x$,

OH_x via the heterojunction interface. Photoinduced electrons were gathered on the $\text{Ti}_3\text{C}_2(\text{O}, \text{OH})_x$ since the CB potential of ZIS was more negative than the Fermi level (E_f) of $\text{Ti}_3\text{C}_2(\text{O}, \text{OH})_x$. The in-plane electrical conductivity of $\text{Ti}_3\text{C}_2(\text{O}, \text{OH})_x$ was at least one order-of-magnitude higher than that vertical to the basal plane [71]. The immobilized O_2 reacted with the accumulated electron at the in-plane of $\text{Ti}_3\text{C}_2\text{T}_x$ to form the $\cdot\text{O}_2^-$ due to more negative potentials than that of the O_2 reduction to $\cdot\text{O}_2^-$ ($E_{\text{O}_2/\cdot\text{O}_2^-} = -0.046 \text{ eV}$). Meanwhile, the $\cdot\text{O}_2^-$ can be reduced to generate the $\cdot\text{OH}$, while the residual holes may directly participate in the degradation reaction of the pollutant.

To detect these radicals in the photocatalytic system, the ESR spin-trap experiments were carried out using the ZIS-MX-8 hybrid under visible light irradiation. In Fig. 14a, the enhanced peak intensity of 5,5-dimethyl-l-pyrroline N-oxide (DMPO)- $\cdot\text{O}_2^-$ in methanol dispersion were linked to the photoinduced generation of $\cdot\text{O}_2^-$. Similar trends

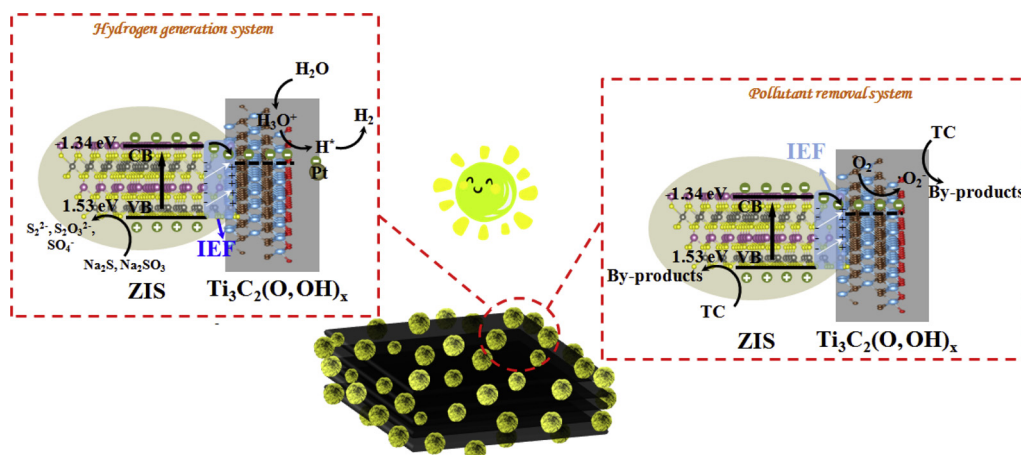


Fig. 13. The proposed mechanism for hydrogen generation and pollutant removal by the $\text{Zn}_2\text{In}_2\text{S}_5/\text{Ti}_3\text{C}_2(\text{O}, \text{OH})_x$ hybrids under visible light illumination.

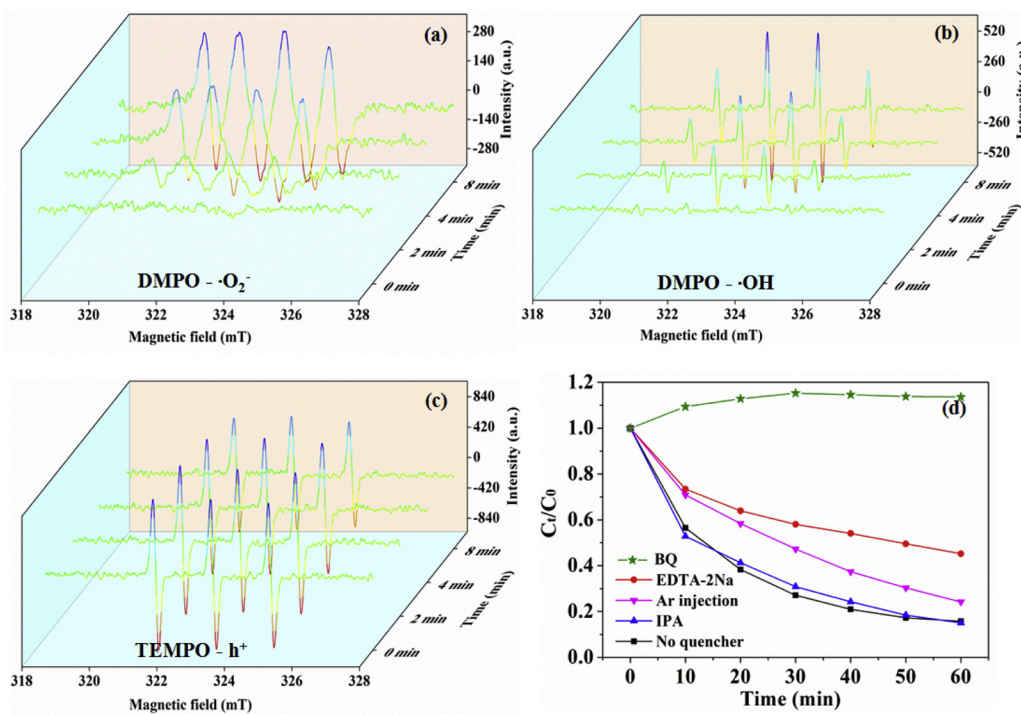
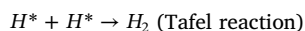
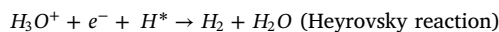
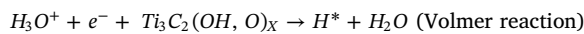


Fig. 14. ESR spectra of radical adducts trapped by DMPO ($\cdot\text{O}_2^-$ and $\cdot\text{OH}$) and TEMPO (h^+) in dispersions under visible light irradiation: (a) in methanol dispersion for DMPO- $\cdot\text{O}_2^-$, (b) in aqueous dispersion for DMPO- $\cdot\text{OH}$ and (c) in aqueous dispersion for TEMPO- h^+ ; (d) effect of different reactive species scavengers on the photodegradation of TC by ZIS-MX-8 under visible-light irradiation.

have appeared (Fig. 14b) after the addition of DMPO in water, indicating the presence of $\cdot\text{OH}$, presumably because of the multiple electron reductive pathways due to the redox reactivity of exposed Ti sites in $\text{Ti}_3\text{C}_2(\text{O}, \text{OH})_x$ [40]. Meanwhile, the gradual disappearance of 2,2,6,6-tetramethyl-1-piperidinyloxy (TEMPO) in Fig. 14c confirms the photogenerated holes. The role of these reactive oxygen species in the photocatalytic degradation of pollutants has also been verified via different trapping experiments (Fig. 14d). The TC degradation was principally dependent on the oxidative species of $\cdot\text{O}_2^-$ or h^+ or both.

2.4.2. Hydrogen generation from water splitting

The ZIS was excited by visible light to produce the electron–hole pairs. Photoinduced electrons were then extracted by $\text{Ti}_3\text{C}_2(\text{OH}, \text{O})_x$ through the coupling interaction between the semiconductive ZIS and metallic $\text{Ti}_3\text{C}_2(\text{O}, \text{OH})_x$, since the CB potential of ZIS was more negative than the Fermi level of $\text{Ti}_3\text{C}_2(\text{O}, \text{OH})_x$. The holes left on the ZIS were reduced by the electron scavenger (Na_2S and Na_2SO_3). In order to understand the interactions between ZIS and metallic $\text{Ti}_3\text{C}_2(\text{O}, \text{OH})_x$ during the hydrogen evolution reaction, the corresponding Tafel plots were constructed in the low current density region. From Fig. S5, a Tafel slope of $\sim 80 \text{ mV dec}^{-1}$ for ZIS-MX-8 is observed, which is significantly lower than that of ZIS (85 mV dec^{-1}). This result also demonstrates that the hydrogen evolution reaction (HER) rate of ZIS-MX-8 nanocomposite was faster than ZIS. The low Tafel slope falls within the range of $40\text{--}120 \text{ mV dec}^{-1}$, suggesting that hydrogen evolution reaction occurred via the Volmer–Heyrovsky mechanism [72,73]. Therefore, the reaction mechanism of hydrogen evolution on the surface of the $\text{Ti}_3\text{C}_2(\text{O}, \text{OH})_x$ can be considered as the following main steps [36]:



With energetically favorable energy, the H_3O^+ ion was adsorbed onto the active sites of $\text{Ti}_3\text{C}_2(\text{O}, \text{OH})_x$ (or Pt nanoparticles) located in the interlayer or edges, and combined with a photoinduced electron to form an H^* atom (Fig. 13). Subsequently, the H^* atom reacted with

another H_3O^+ ion from water and an electron from $\text{Ti}_3\text{C}_2(\text{O}, \text{OH})_x$ (or Pt nanoparticles) to generate a H_2 molecule. With the gradual accumulation of H, hydrogen was released when the H coverage reached 4/8 (adsorption of atomic hydrogen on $\text{Ti}_3\text{C}_2(\text{O}, \text{OH})_x$), which resulted when the $|\Delta G_{\text{H}^*}|$ for atomic hydrogen adsorption was very close to 0 [34,74]. Remotely separated H^* atoms are usually energetically favorable to migrate closer to form hydrogen molecules via the Tafel reaction [75]. However, it has been theoretically reported that the energy barrier of the Heyrovsky step was only 0.29 eV, which is much smaller than that of the Tafel step (0.99 eV) [74]. Therefore, the hydrogen evolution in the ZIS-MX composite follows the Volmer reaction and Heyrovsky mechanism in the presence of photogenerated electrons and H_3O^+ ions at the active sites ($-\text{O}$ surface terminations). In addition, with the aid of the quasi-alloying effect, a weaker bonding to electropositive species (i.e. H_3O^+ and H^*) at the interface facilitated the quick dissociation and spill of hydrogen, which further enhanced the H_2 generation.

3. Conclusions

In summary, hierarchical $\text{Zn}_2\text{In}_2\text{S}_5/\text{Ti}_3\text{C}_2(\text{O}, \text{OH})_x$ was rationally constructed using $\text{Ti}_3\text{C}_2(\text{O}, \text{OH})_x$ as a 2D platform for *in situ* growth of the flower-like $\text{Zn}_2\text{In}_2\text{S}_5$ microsphere under anaerobically hydrothermal condition. The $\text{Zn}_2\text{In}_2\text{S}_5/\text{Ti}_3\text{C}_2(\text{O}, \text{OH})_x$ heterostructured hybrids with the $\text{Ti}_3\text{C}_2(\text{O}, \text{OH})_x$ content of 1.5% (by mass) exhibited (i) boosted visible-light photocatalytic TC degradation efficiency, which was ~ 1.25 times higher than those of pure $\text{Zn}_2\text{In}_2\text{S}_5$; and (ii) more efficient visible-light photocatalytic H_2 generation ($12,983.8 \mu\text{mol g}^{-1}$), that was significantly enhanced by 1.97 times with respect to $\text{Zn}_2\text{In}_2\text{S}_5$. On the surface of hybrids, hydrogen evolution follows the Volmer reaction and Heyrovsky mechanism in the presence of photogenerated electrons and H_3O^+ ions at the active sites ($-\text{O}$ surface terminations). The apparent quantum efficiency of ZIS-MX-8 was 8.96% at 420 nm. Moreover, the photocatalytic removal performance was improved with the increase of temperature in the range of 35–55 °C. The addition of $\text{Ti}_3\text{C}_2(\text{O}, \text{OH})_x$ facilitated the separation and transfer of photogenerated charge carriers via interfacial-built-in quasi-alloying effect and led to the efficient electron transfer from the $\text{Zn}_2\text{In}_2\text{S}_5$ to the $\text{Ti}_3\text{C}_2(\text{O}, \text{OH})_x$ with an improved electron-transfer efficiency of 33.0%. This work is expected to

be valuable towards the development of hierarchical MXene-based photocatalysts for solar utilization and environmental remediation.

4. Experimental section

The detailed experiments have been shown in Supporting Information.

Acknowledgments

The authors gratefully acknowledge the financial support provided by the Singapore Ministry of Education Academic Research Funds Tier 2 (MOE2014-T2-2-074; ARC16/15) and Tier 1 (2015-T1-001-023; RG7/15), the GSK (GlaxoSmithKline) – EDB (Economic Development Board) Trust Fund, and the Joint Singapore-Germany Research Project Fund (SGP-PROG3-019). We also acknowledge funding from the Projects of the National Nature Science Foundation of China (No. 21776066, 51708195). Hou Wang, Yuanmiao Sun and Yan Wu contributed equally to this work.

Appendix A. Supplementary data

Supplementary material related to this article can be found, in the online version, at doi:<https://doi.org/10.1016/j.apcatb.2018.12.051>.

References

- J. Liu, Y. Liu, N. Liu, Y. Han, X. Zhang, H. Huang, Y. Lifshitz, S.-T. Lee, J. Zhong, Z. Kang, Metal-free efficient photocatalyst for stable visible water splitting via a two-electron pathway, *Science* 347 (2015) 970–974.
- H. Wang, Y. Wu, X. Yuan, G. Zeng, J. Zhou, X. Wang, J.W. Chew, Clay-inspired MXene-based electrochemical devices and photo-electrocatalyst: state-of-the-art progresses and challenges, *Adv. Mater.* 30 (2018) 1704561.
- A. Fujishima, K. Honda, Electrochemical photolysis of water at a semiconductor electrode, *Nature* 238 (1972) 37.
- H. Wang, Y. Wu, M. Feng, W. Tu, T. Xiao, T. Xiong, H. Ang, X. Yuan, J.W. Chew, Visible-light-driven removal of tetracycline antibiotics and reclamation of hydrogen energy from natural water matrices and wastewater by polymeric carbon nitride foam, *Water Res.* 144 (2018) 215–225.
- S. Wang, X. Wang, Multifunctional metal–organic frameworks for photocatalysis, *Small* 11 (2015) 3097–3112.
- G. Zhang, M. Zhang, X. Ye, X. Qiu, S. Lin, X. Wang, Iodine modified carbon nitride semiconductors as visible light photocatalysts for hydrogen evolution, *Adv. Mater.* 26 (2014) 805–809.
- G. Zhang, L. Lin, G. Li, Y. Zhang, A. Savateev, S. Zafeiratos, X. Wang, M. Antonietti, Ionothermal synthesis of triazine-heptazine-based copolymers with apparent quantum yields of 60 % at 420 nm for solar hydrogen production from “Sea Water”, *Angew. Chem. Int. Ed. Engl.* 57 (2018) 9372–9376.
- G. Zhang, Z.-A. Lan, X. Wang, Conjugated polymers: catalysts for photocatalytic hydrogen evolution, *Angew. Chem. Int. Ed. Engl.* 55 (2016) 15712–15727.
- M. Ou, W. Tu, S. Yin, W. Xing, S. Wu, H. Wang, S. Wan, Q. Zhong, R. Xu, Amino-assisted anchoring of CsPbBr₃ perovskite quantum dots on porous g-C₃N₄ for enhanced photocatalytic CO₂ reduction, *Angew. Chem. Int. Ed. Engl.* 57 (2018) 13570–13574.
- F.M. Zhang, J.L. Sheng, Z.D. Yang, X.J. Sun, H.L. Tang, M. Lu, H. Dong, F.C. Shen, J. Liu, Y.-Q. Lan, Rational design of MOF/COF hybrid materials for photocatalytic H₂ evolution in the presence of sacrificial electron donors, *Angew. Chem. Int. Ed. Engl.* 57 (2018) 12106–12110.
- S. Wang, B.Y. Guan, Y. Lu, X.W.D. Lou, Formation of hierarchical In₂S₃–CdIn₂S₄ heterostructured nanotubes for efficient and stable visible light CO₂ reduction, *J. Am. Chem. Soc.* 139 (2017) 17305–17308.
- Y. Pan, X. Yuan, L. Jiang, H. Yu, J. Zhang, H. Wang, R. Guan, G. Zeng, Recent advances in synthesis, modification and photocatalytic applications of micro/nano-structured zinc indium sulfide, *Chem. Eng. J.* 354 (2018) 407–431.
- S. Shen, L. Zhao, L. Guo, Zn_nIn₂S_{3+m} (m = 1–5, integer): A new series of visible-light-driven photocatalysts for splitting water to hydrogen, *Int. J. Hydrogen Energy* 35 (2010) 10148–10154.
- S. Shen, L. Zhao, Z. Zhou, L. Guo, Enhanced photocatalytic hydrogen evolution over Cu-doped ZnIn₂S₄ under visible light irradiation, *J. Phys. Chem. C* 112 (2008) 16148–16155.
- S. Wang, B.Y. Guan, X. Wang, X.W.D. Lou, Formation of hierarchical Co₉S₈@ZnIn₂S₄ heterostructured cages as an efficient photocatalyst for hydrogen evolution, *J. Am. Chem. Soc.* 140 (2018) 15145–15148.
- W. Yang, L. Zhang, J. Xie, X. Zhang, Q. Liu, T. Yao, S. Wei, Q. Zhang, Y. Xie, Enhanced photoexcited carrier separation in oxygen-doped ZnIn₂S₄ nanosheets for hydrogen evolution, *Angew. Chem. Int. Ed. Engl.* 55 (2016) 6716–6720.
- X. Jiao, Z. Chen, X. Li, Y. Sun, S. Gao, W. Yan, C. Wang, Q. Zhang, Y. Lin, Y. Luo, Y. Xie, Defect-mediated electron-hole separation in one-unit-cell ZnIn₂S₄ layers for boosted solar-driven CO₂ reduction, *J. Am. Chem. Soc.* 139 (2017) 7586–7594.
- S. Zhang, X. Liu, C. Liu, S. Luo, L. Wang, T. Cai, Y. Zeng, J. Yuan, W. Dong, Y. Pei, Y. Liu, MoS₂ quantum dot growth induced by S vacancies in a ZnIn₂S₄ monolayer: atomic-level heterostructure for photocatalytic hydrogen production, *ACS Nano* 12 (2018) 751–758.
- S. Wang, B.Y. Guan, X.W.D. Lou, Construction of ZnIn₂S₄–In₂O₃ hierarchical tubular heterostructures for efficient CO₂ photoreduction, *J. Am. Chem. Soc.* 140 (2018) 5037–5040.
- X. Li, Y. Cheng, Q. Wu, J. Xu, Y. Wang, Synergistic effect of the rearranged sulfur vacancies and sulfur interstitials for 13-fold enhanced photocatalytic H₂ production over defective Zn₂In₂S₅ nanosheets, *Appl. Catal. B: Environ.* 240 (2019) 270–276.
- I. Poulios, N. Papadopoulos, Photoelectrochemical behaviour of Zn₃In₂S₆ single crystals in aqueous solutions, *Sol. Energy Mater.* 20 (1990) 43–51.
- J. Song, C. Ma, W. Zhang, S. Yang, S. Wang, L. Lv, L. Zhu, R. Xia, X. Xu, Tumor cell-targeted Zn₃In₂S₆ and Ag–Zn–In–S quantum dots for color adjustable luminophores, *J. Mater. Chem. B* 4 (2016) 7909–7918.
- Y. Wu, H. Wang, W. Tu, Y. Liu, S. Wu, Y.Z. Tan, J.W. Chew, Construction of hierarchical 2D–2D Zn₃In₂S₆/fluorinated polymeric carbon nitride nanosheets photocatalyst for boosting photocatalytic degradation and hydrogen production performance, *Appl. Catal. B: Environ.* 233 (2018) 58–69.
- B. Anasori, M.R. Lukatskaya, Y. Gogotsi, 2D metal carbides and nitrides (MXenes) for energy storage, *Nat. Rev. Mater.* 2 (2017) 16098.
- Q. Peng, J. Guo, Q. Zhang, J. Xiang, B. Liu, A. Zhou, R. Liu, Y. Tian, Unique lead adsorption behavior of activated hydroxyl group in two-dimensional titanium carbide, *J. Am. Chem. Soc.* 136 (2014) 4113–4116.
- L. Ding, Y. Wei, Y. Wang, H. Chen, J. Caro, H. Wang, A two-dimensional lamellar membrane: MXene nanosheet stacks, *Angew. Chem. Int. Ed. Engl.* 56 (2017) 1825–1829.
- J. Pang, R.G. Mendes, A. Bachmatiuk, L. Zhao, H.Q. Ta, T. Gemming, H. Liu, Z. Liu, M.H. Rummeli, Applications of 2D MXenes in energy conversion and storage systems, *Chem. Soc. Rev.* (2019), <https://doi.org/10.1039/C8CS00324F>.
- M. Ghidui, M.R. Lukatskaya, M.Q. Zhao, Y. Gogotsi, M.W. Baroum, Conductive two-dimensional titanium carbide ‘clay’ with high volumetric capacitance, *Nature* 516 (2014) 78–81.
- F. Shahzad, M. Alhabeb, C.B. Hatter, B. Anasori, S.M. Hong, C.M. Koo, Y. Gogotsi, Electromagnetic interference shielding with 2D transition metal carbides (MXenes), *Science* 353 (2016) 1137–1140.
- M.R. Lukatskaya, O. Mashtalir, C.E. Ren, Y. Dall’Agnese, P. Rozier, P.L. Taberna, M. Naguib, P. Simon, M.W. Baroum, Y. Gogotsi, Cation intercalation and high volumetric capacitance of two-dimensional titanium carbide, *Science* 341 (2013) 1502–1505.
- Y. Wang, Y. Li, Z. Qiu, X. Wu, P. Zhou, T. Zhou, J. Zhao, Z. Miao, J. Zhou, S. Zhuo, Fe₃O₄@Ti₃C₂ MXene hybrids with ultrahigh volumetric capacity as an anode material for lithium-ion batteries, *J. Mater. Chem. A* 6 (2018) 11189–11197.
- M. Khazaei, A. Ranjbar, M. Arai, T. Sasaki, S. Yunoki, Electronic properties and applications of MXenes: a theoretical review, *J. Mater. Chem. C* 5 (2017) 2488–2503.
- L. Zhao, B. Dong, S. Li, L. Zhou, L. Lai, Z. Wang, S. Zhao, M. Han, K. Gao, M. Lu, X. Xie, B. Chen, Z. Liu, X. Wang, H. Zhang, H. Li, J. Liu, H. Zhang, X. Huang, W. Huang, Inter-diffusion reaction assisted hybridization of two-dimensional metal-organic frameworks and Ti₃C₂T_x nanosheets for electrocatalytic oxygen evolution, *ACS Nano* 11 (2017) 5800–5807.
- J. Ran, G. Gao, F.T. Li, T.Y. Ma, A. Du, S.Z. Qiao, Ti₃C₂ MXene co-catalyst on metal sulfide photo-absorbers for enhanced visible-light photocatalytic hydrogen production, *Nat. Commun.* 8 (2017) 13907.
- X. Xie, N. Zhang, Z.-R. Tang, M. Anpo, Y.-J. Xu, Ti₃C₂T_x MXene as a Janus cocatalyst for concurrent promoted photoactivity and inhibited photocorrosion, *Appl. Catal. B: Environ.* 237 (2018) 43–49.
- Y. Sun, D. Jin, Y. Sun, X. Meng, Y. Gao, Y. Dall’Agnese, G. Chen, X.-F. Wang, g-C₃N₄/Ti₃C₂T_x (MXenes) composite with oxidized surface groups for efficient photocatalytic hydrogen evolution, *J. Mater. Chem. A* 6 (2018) 9124–9131.
- X. An, W. Wang, J. Wang, H. Duan, J. Shi, X. Yu, The synergistic effects of Ti₃C₂ MXene and Pt as co-catalysts for highly efficient photocatalytic hydrogen evolution over g-C₃N₄, *Phys. Chem. Chem. Phys.* 20 (2018) 11405–11411.
- Y. Xu, S. Wang, J. Yang, B. Han, R. Nie, J. Wang, Y. Dong, X. Yu, J. Wang, H. Jing, Highly efficient photoelectrocatalytic reduction of CO₂ on the Ti₃C₂/g-C₃N₄ heterojunction with rich Ti³⁺ and pyri-N species, *J. Mater. Chem. A* 6 (2018) 15213–15220.
- S. Cao, B. Shen, T. Tong, J. Fu, J. Yu, 2D/2D heterojunction of ultrathin MXene/Bi₂WO₆ nanosheets for improved photocatalytic CO₂ reduction, *Adv. Funct. Mater.* 28 (2018) 1800136.
- T. Cai, L. Wang, Y. Liu, S. Zhang, W. Dong, H. Chen, X. Yi, J. Yuan, X. Xia, C. Liu, S. Luo, Ag₃PO₄/Ti₃C₂ MXene interface materials as a Schottky catalyst with enhanced photocatalytic activities and anti-photocorrosion performance, *Appl. Catal. B: Environ.* 239 (2018) 545–554.
- C. Peng, X. Yang, Y. Li, H. Yu, H. Wang, F. Peng, Hybrids of two-dimensional Ti₃C₂ and TiO₂ exposing {001} facets toward enhanced photocatalytic activity, *ACS Appl. Mater. Inter.* 8 (2016) 6051–6060.
- M. Ye, X. Wang, E. Liu, J. Ye, D. Wang, Boosting the photocatalytic activity of P25 for carbon dioxide reduction by using a surface-alkalinized titanium carbide MXene as cocatalyst, *ChemSusChem* 11 (2018) 1606–1611.
- J. Low, L. Zhang, T. Tong, B. Shen, J. Yu, TiO₂/MXene Ti₃C₂ composite with excellent photocatalytic CO₂ reduction activity, *J. Catal.* 361 (2018) 255–266.
- O. Mashtalir, M. Naguib, V.N. Mochalin, Y. Dall’Agnese, M. Heon, M.W. Baroum, Y. Gogotsi, Intercalation and delamination of layered carbides and carbonitrides,

Nat. Commun. 4 (2013) 1716.

[45] H. Wang, Y. Wu, T. Xiao, X. Yuan, G. Zeng, W. Tu, S. Wu, H.Y. Lee, Y.Z. Tan, J.W. Chew, Formation of quasi-core-shell In_2S_3 /anatase TiO_2 @metallic $\text{Ti}_3\text{C}_2\text{T}_x$ hybrids with favorable charge transfer channels for excellent visible-light-photo-catalytic performance, *Appl. Catal. B: Environ.* 233 (2018) 213–225.

[46] J. Ran, W. Guo, H. Wang, B. Zhu, J. Yu, S.Z. Qiao, Metal-free 2D/2D phosphorene-g- C_3N_4 Van der Waals heterojunction for highly enhanced visible-light photo-catalytic H_2 production, *Adv. Mater.* 30 (2018) 1800128.

[47] J. Luo, W. Zhang, H. Yuan, C. Jin, L. Zhang, H. Huang, C. Liang, Y. Xia, J. Zhang, Y. Gan, X. Tao, Pillared structure design of MXene with ultralarge interlayer spacing for high-performance lithium-ion capacitors, *ACS Nano* 11 (2017) 2459–2469.

[48] M.D. Levi, M.R. Lukatskaya, S. Sigalov, M. Beidaghi, N. Shpigel, L. Daikhin, D. Aurbach, M.W. Barsoum, Y. Gogotsi, Solving the capacitive paradox of 2D MXene using electrochemical quartz-crystal admittance and in situ electronic conductance measurements, *Adv. Energy Mater.* 5 (2015) 1400815.

[49] H. Wang, X. Yuan, Y. Wu, G. Zeng, H. Dong, X. Chen, L. Leng, Z. Wu, L. Peng, In situ synthesis of In_2S_3 @MIL-125(Ti) core-shell microparticle for the removal of tetracycline from wastewater by integrated adsorption and visible-light-driven photo-catalysis, *Appl. Catal. B: Environ.* 186 (2016) 19–29.

[50] J. Halim, S. Kota, M.R. Lukatskaya, M. Naguib, M.-Q. Zhao, E.J. Moon, J. Pitock, J. Nanda, S.J. May, Y. Gogotsi, M.W. Barsoum, Synthesis and characterization of 2D molybdenum carbide (MXene), *Adv. Funct. Mater.* 26 (2016) 3118–3127.

[51] Y. Wei, X. Wu, Y. Zhao, L. Wang, Z. Zhao, X. Huang, J. Liu, J. Li, Efficient photo-catalysts of TiO_2 nanocrystals-supported PtRu alloy nanoparticles for CO_2 reduction with H_2O : synergistic effect of Pt-Ru, *Appl. Catal. B: Environ.* 236 (2018) 445–457.

[52] H. Liu, M. Wang, X. Zhang, J. Ma, G. Lu, High efficient photocatalytic hydrogen evolution from formaldehyde over sensitized Ag@Ag-Pd alloy catalyst under visible light irradiation, *Appl. Catal. B: Environ.* 237 (2018) 563–573.

[53] M.R. Knecht, M.G. Weir, A.I. Frenkel, R.M. Crooks, Structural rearrangement of bimetallic alloy PdAu nanoparticles within dendrimer templates to yield core/shell configurations, *Chem. Mater.* 20 (2008) 1019–1028.

[54] S. Cao, Y. Chen, H. Wang, J. Chen, X. Shi, H. Li, P. Cheng, X. Liu, M. Liu, L. Piao, Ultrasmall CoP nanoparticles as efficient cocatalysts for photocatalytic formic acid dehydrogenation, *Joule* 2 (2018) 549–557.

[55] Z. Lei, W. You, M. Liu, G. Zhou, T. Takata, M. Hara, K. Domen, C. Li, Photocatalytic water reduction under visible light on a novel ZnIn_2S_4 catalyst synthesized by hydrothermal method, *Chem. Commun.* 0 (2003) 2142–2143.

[56] R. Li, L. Zhang, L. Shi, P. Wang, MXene Ti_3C_2 : an effective 2D light-to-Heat conversion material, *ACS Nano* 11 (2017) 3752–3759.

[57] Z. Gan, X. Wu, M. Meng, X. Zhu, L. Yang, P.K. Chu, Photothermal contribution to enhanced photocatalytic performance of graphene-based nanocomposites, *ACS Nano* 8 (2014) 9304–9310.

[58] Z. Jiang, W. Wan, H. Li, S. Yuan, H. Zhao, P.K. Wong, A hierarchical Z-scheme α - Fe_2O_3 /g- C_3N_4 hybrid for enhanced photocatalytic CO_2 reduction, *Adv. Mater.* 30 (2018) 1706108.

[59] Y. Wu, H. Wang, Y. Sun, T. Xiao, W. Tu, X. Yuan, G. Zeng, S. Li, J.W. Chew, Photogenerated charge transfer via interfacial internal electric field for significantly improved photocatalysis in direct Z-scheme oxygen-doped carbon nitrogen/CoAl-layered double hydroxide heterojunction, *Appl. Catal. B: Environ.* 227 (2018) 530–540.

[60] J. Lee, H.S. Shim, M. Lee, J.K. Song, D. Lee, Size-controlled electron transfer and photocatalytic activity of ZnO -Au nanoparticle composites, *J. Phys. Chem. Lett.* 2 (2011) 2840–2845.

[61] K. Tvrdy, P.A. Frantsuzov, P.V. Kamat, Photoinduced electron transfer from semiconductor quantum dots to metal oxide nanoparticles, *Proc. Natl. Acad. Sci. U. S. A.* 108 (2011) 29–34.

[62] H.-i. Kim, D. Monllor-Satoca, W. Kim, W. Choi, N-doped TiO_2 nanotubes coated with a thin TaO_xN_y layer for photoelectrochemical water splitting: dual bulk and surface modification of photoanodes, *Energy Environ. Sci.* 8 (2015) 247–257.

[63] J.X. Feng, J.Q. Wu, Y.X. Tong, G.R. Li, Efficient hydrogen evolution on Cu nanodots-decorated Ni_3S_2 nanotubes by optimizing atomic hydrogen adsorption and desorption, *J. Am. Chem. Soc.* 140 (2018) 610–617.

[64] M.T. Greiner, T.E. Jones, S. Beeg, L. Zwiener, M. Scherzer, F. Girsdsies, S. Piccinin, M. Armbrüster, A. Knop-Gericke, R. Schlögl, Free-atom-like d states in single-atom alloy catalysts, *Nat. Chem.* 10 (2018) 1008–1015.

[65] P.E. Blöchl, Projector augmented-wave method, *Phys. Rev. B* 50 (1994) 17953–17979.

[66] P. Hu, C.K. Ngaw, Y. Yuan, P.S. Bassi, S.C. Joachim Loo, T.T. Yang Tan, Bandgap engineering of ternary sulfide nanocrystals by solution proton alloying for efficient photocatalytic H_2 evolution, *Nano Energy* 26 (2016) 577–585.

[67] L. Jiang, X. Yuan, Y. Pan, J. Liang, G. Zeng, Z. Wu, H. Wang, Doping of graphitic carbon nitride for photocatalysis: a review, *Appl. Catal. B: Environ.* 217 (2017) 388–406.

[68] C.C. Chen, W.H. Ma, J.C. Zhao, Semiconductor-mediated photodegradation of pollutants under visible-light irradiation, *Chem. Soc. Rev.* 39 (2010) 4206–4219.

[69] X. Sang, Y. Xie, M.W. Lin, M. Alhabeb, K.L. Van Aken, Y. Gogotsi, P.R. Kent, K. Xiao, R.R. Uocic, Atomic defects in monolayer titanium carbide ($\text{Ti}_3\text{C}_2\text{T}_x$) MXene, *ACS Nano* 10 (2016) 9193–9200.

[70] E. Lira, S. Wendt, P. Huo, J.Ø. Hansen, R. Streber, S. Porsgaard, Y. Wei, R. Bechstein, E. Lægsgaard, F. Besenbacher, The importance of bulk Ti^{3+} Defects in the oxygen chemistry on titania surfaces, *J. Am. Chem. Soc.* 133 (2011) 6529–6532.

[71] T. Hu, H. Zhang, J. Wang, Z. Li, M. Hu, J. Tan, P. Hou, F. Li, X. Wang, Anisotropic electronic conduction in stacked two-dimensional titanium carbide, *Sci. Rep.* 5 (2015) 16329.

[72] X. Hao, J. Zhou, Z. Cui, Y. Wang, Y. Wang, Z. Zou, Zn-vacancy mediated electron-hole separation in ZnS /g- C_3N_4 heterojunction for efficient visible-light photo-catalytic hydrogen production, *Appl. Catal. B: Environ.* 229 (2018) 41–51.

[73] X. Hao, Z. Cui, J. Zhou, Y. Wang, Y. Hu, Y. Wang, Z. Zou, Architecture of high efficient zinc vacancy mediated Z-scheme photocatalyst from metal-organic frameworks, *Nano Energy* 52 (2018) 105–116.

[74] G. Gao, A.P. O'Mullane, A. Du, 2D MXenes: a new family of promising catalysts for the hydrogen evolution reaction, *ACS Catal.* 7 (2016) 494–500.

[75] Z. Guo, J. Zhou, L. Zhu, Z. Sun, MXene: a promising photocatalyst for water splitting, *J. Mater. Chem. A* 4 (2016) 11446–11452.